Investigation into the Efficiency Gap between Krypton and Xenon Operation on a Magnetically Shielded Hall Thruster

Leanne L. Su *, Thomas A. Marks †, and Benjamin A. Jorns ‡
University of Michigan, Ann Arbor, MI, 48109

Axial ion velocity profiles were measured along channel centerline of a 9-kW class magnetically shielded Hall thruster operating on both krypton and xenon at multiple discharge powers. These profiles were used to calibrate multi-fluid simulations in Hall2De for the 300 V, 15 A and 600 V, 15 A conditions, resulting in minimal differences in the velocity profiles and matching discharge currents within 2 A. Results from the calibrated simulations are used to calculate the ion production rates for each propellant, revealing a larger increase in the ion production rate per unit volume for xenon between 300 V and 600 V than for krypton. This disparity may be the cause for the increased efficiency gap at high voltages between the propellants, a theory supported through calculations of efficiency ratio between propellants at each voltage.

Nomenclature

$\dot{m}_a$	Anode neutral mass flow [kg/s]
$\dot{m}_b$	Beam ion mass flow [kg/s]
$\dot{n}_i$	Rate of ion production per unit volume [m^{-3}s^{-1}]
η_a	Anode efficiency
η_m	Mass utilization efficiency
ν_{an}	Anomalous electron collision frequency [s^{-1}]
ν_e	Electron collision frequency [s^{-1}]
Ω_e	Hall parameter
ω_{ce}	Electron gyrofrequency [s^{-1}]
σ_{iz}	Ionization cross-section [m^{-2}]
ε	Energy [eV]
B	Magnetic field [G]
E	Electric field [V/m]
I_d	Discharge current [A]
j_e	Electron current density [A/m]
k_{iz}	Ionization rate coefficient [m^3/s]
L_{ch}	Channel length [m]
m_e	Electron mass [kg]
m_i	Ion mass [kg]
n_e	Electron density [m^{-3}]
n_n	Neutral density [m^{-3}]
q	Fundamental charge [C]
r	Radial position [m]
T_e	Electron temperature [eV]
u_e	Electron velocity [m/s]
u_i	Ion velocity [m/s]
V_d	Discharge voltage [V]
z	Axial position [m]

*Ph.D. Candidate, Aerospace Engineering, AIAA Student Member
†Ph.D. Candidate, Aerospace Engineering, AIAA Student Member
‡Associate Professor, Aerospace Engineering, AIAA Associate Fellow

I. Introduction

Hall thrusters are a promising candidate technology for scaling to the high powers and long lifetimes required for crewed and robotic exploration of deep space [1]. With that said, one of the remaining barriers towards using Hall thrusters for deep space travel is the availability of propellant. Traditionally, the propellant of choice on Hall thrusters has been xenon due to its low ionization energy and high mass. However, xenon is greatly limited in the atmosphere, and estimates suggest that a crewed Mars mission would require more than 10% of the annual global xenon production [2]. Additionally, this scarcity makes the price of xenon both expensive and highly variable. In fall of 2021, xenon was $74/L, while in spring of 2022, the price rose to $171/L.

A potential alternative to xenon is krypton, which is nearly ten times less expensive and more readily available in the atmosphere. Krypton has been extensively investigated as a Hall thruster propellant, with multiple studies indicating that the anode efficiency of Hall thrusters operating on krypton is 5–15% lower than that of xenon at the same conditions [3–9]. This difference in efficiency has primarily been attributed to the lower mass utilization of krypton [5–10], a measure of how efficiently a thruster ionizes neutrals flowing into its anode. It should be noted that most of these studies were performed on thrusters designed for xenon and not krypton. With thrusters specifically designed for krypton [8], the efficiency gap closes to within 10%. With the advent of SpaceX's Starlink constellation, krypton has become the dominant in-space propellant for Hall thrusters, with thousands of operational satellites currently in orbit.

While most studies on krypton operation have been confined to Hall thrusters based on traditional magnetic topologies, there has been a recent development in Hall thruster technology known as magnetic shielding. Magnetic shielding is a technique that greatly increases thruster lifetimes by shaping the magnetic fields such that energetic ions are directed away from the channel walls [11, 12]. However, there has been limited investigation into how magnetically shielded thrusters perform on krypton. In light of the advantages of shielding as well as krypton, there is a need to assess if there are adverse consequences of running a shielded thruster on krypton.

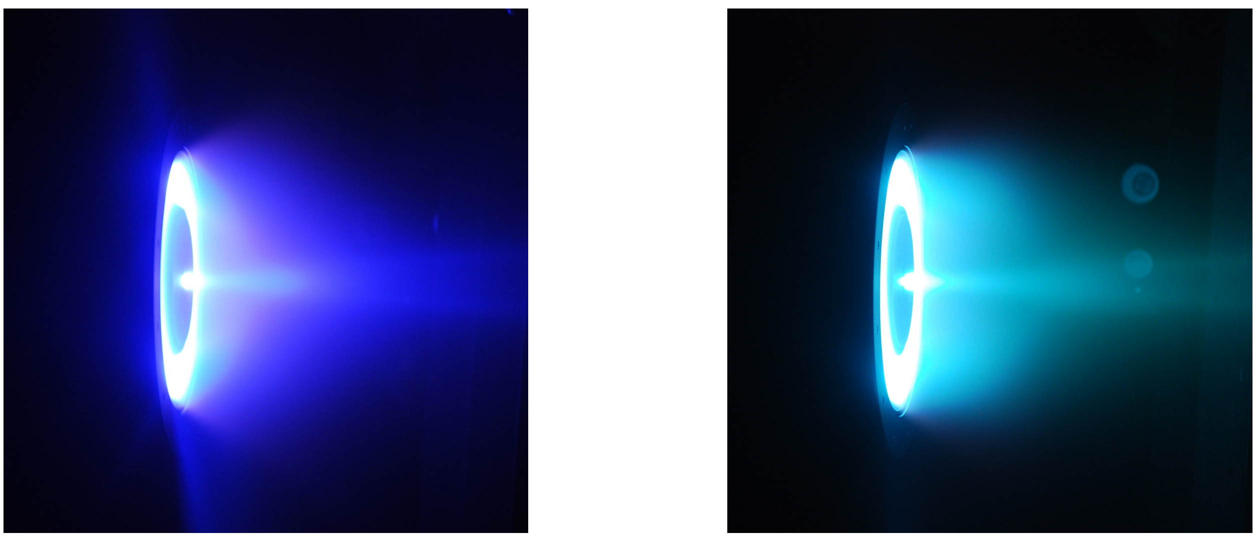

(a) (b)

Fig. 1 H9 operating at 300 V, 15 A using a) krypton and b) xenon propellant [13].

To this end, we recently investigated the impact on the performance of a magnetically shielded thruster designed for xenon but operated on krypton. In line with previous work, we found that the efficiency was 9-18% lower with krypton than with xenon, with much of this discrepancy attributable to low mass utilization [13]. However, unlike in previous studies of unshielded thrusters where the efficiency gap between xenon and krypton operation decreased at higher voltages [5], this efficiency gap expanded on a magnetically shielded thruster. In Ref. [13], we theorized that this difference in behavior was due to the higher channel centerline temperature of shielded thrusters and the non-linearity of ionization cross-section, a conjecture informed by downstream and global measurements.

This hypothesis is difficult to confirm without direct measurements of the internal properties of the thruster. Such measurements are unfeasible to obtain with probes due to the perturbations they cause in the plasma [14]. One alternative, commonly employed at JPL, is to calibrate a high-fidelity two-dimensional model of the thruster [15] with measurements of ion velocities along channel centerline. These velocity measurements are obtained via laser-induced fluorescence (LIF), a non-invasive optical diagnostic [16, 17]. Once the model is validated against experimental data, we treat its predictions of the plasma conditions inside the channel as indirect measurements of the real thruster.

The goal of this work is to investigate the differences in plasma parameters underlying the gap in between krypton and xenon efficiency on a shielded thruster. We do so by employing laser-induced fluorescence measurements combined with the JPL-developed multi-fluid Hall thruster code, Hall2De [18]. This paper is organized as follows. In Sec. II, we detail both the experimental setup used, including the thruster, vacuum facility, and diagnostics, as well as the simulation software and setup. We then present in Sec. III the ion velocity distribution functions obtained from LIF measurements as well as results from the Hall2De simulations and how they compare to experimental data. Next, in Sec. IV we discuss our results in context of scaling laws for acceleration regions at high powers and in context of what physical mechanisms appear to be driving the gap in performance between krypton and xenon operation at high voltages. Finally, in Sec. V, we summarize our findings and comment on the underlying physics of magnetically shielded Hall thrusters using krypton.

II. Methodology

In this section, we describe both the experimental and simulation tools used to determine variosu plasma parameters in our investigation of plasma properties within the Hall thruster.

A. Experimental setup

1. Thruster and facility

Our test article for this campaign was the H9, a 9-kW magnetically shielded Hall thruster developed in partnership between the University of Michigan (UM), the Jet Propulsion Laboratory (JPL), and the Air Force Research Laboratory (AFRL) [19, 20]. We used a centrally-mounted LaB6 cathode [21] operating at a fixed 7% cathode flow fraction with the cathode electrically tied to the body and isolated from facility ground [22] at all conditions. A number of thermocouples were attached to the H9 at various locations to monitor thruster health. We operated the H9 in the Large Vacuum Test Facility, a chamber 6 m in diameter and 9 m in length, which is capable of pumping ~500 kL/s of xenon and ~600 kL/s of krypton [23]. Pressures in the chamber were measured with a Stabil ion gauge calibrated for xenon, mounted 1 m away from the thruster in the thruster exit plane following industry standards [24]. This thruster is operated with krypton and xenon propellant (see Fig. 1).

2. Operating conditions

Voltage (V)	Current (A)	Power (kW)
300	15	4.5
300	20	6
300	30	9
400	15	6
600	15	9

Table 1 Operating conditions for the H9 on krypton and xenon.

We operate the H9 at five different conditions on krypton and on xenon. The 300 V, 15 A (4.5 kW) condition is our baseline for comparison, with high-current and high-voltage conditions at 6 and 9 kW (Table 1). The current was adjusted by changing the flow through the anode and cathode.

3. Diagnostics

Laser-induced fluorescence is a non-invasive technique for measuring the ion velocity distribution of a given species. A metastable state of an ion is non-resonantly excited with a laser at some wavelength, and the resulting fluorescence is measured to indicate the density of that population. By detuning the injection laser from the central wavelength, we can take advantage of the Doppler effect to measure the relative density of a species traveling at different velocities based on the intensity of its fluorescence. This results in a velocity distribution function (VDF) at a point in space [16, 17].

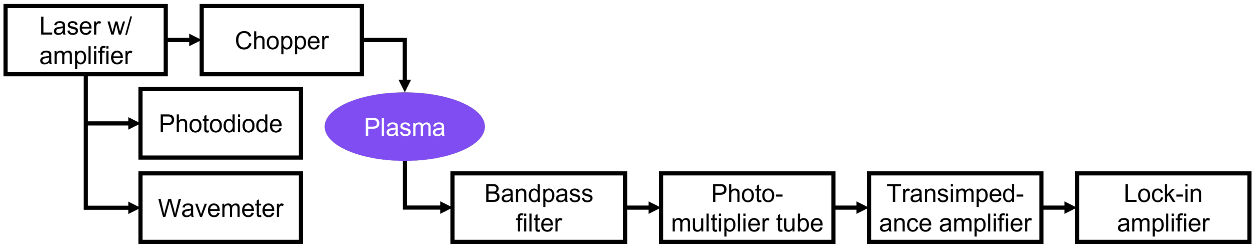

Fig. 2 System overview of laser-induced fluorescence.

We selected the Kr II transition at 728.982 nm in air that fluoresces at 473.9 nm, a non-resonant transition that has relatively high intensity [25] and has been used previously for LIF of Hall thrusters to measure singly-ionized krypton populations [26]. A TOPTICA TApro tunable diode laser and tapered amplifier system was configured to inject into the plasma with a center wavelength of 729.18 nm in vacuum with a maximum output power of 500 mW and a mode hop free tuning range of 56 GHz. An internal photodiode monitored the output power, while a probe beam from the laser was precisely measured by a HighFinesse WS-7 wavemeter. The main beam from the laser was passed through a SR540 mechanical chopper operating at 2 kHz before being injected into the chamber through a fiber.

Species	Excitation λ, air (nm)	Fluorescence λ (nm)
Kr II	728.982	473.90
Xe II	834.72	541.91

Table 2 Excitation and fluorescence wavelengths for singly-ionized krypton and singly-ionized xenon.

For the Xe II setup, we used the 834.72 nm in air, 834.935 in vacuum transition that fluoresces at 541.91 nm [25], the same transition used for previous xenon measurements [27]. Light from a Newport TLB-6700 diode laser was passed through a TA-7600-LN tapered amplifier. Two beam samplers were used to split off a small amount to light to ThorLabs PDA36A photodiode that measured the output power and to the same wavemeter as used for the krypton setup. The remaining light was passed through the same chopper and follows the same path for the rest of the system. The general setup of the LIF system can be seen in Fig. 2.

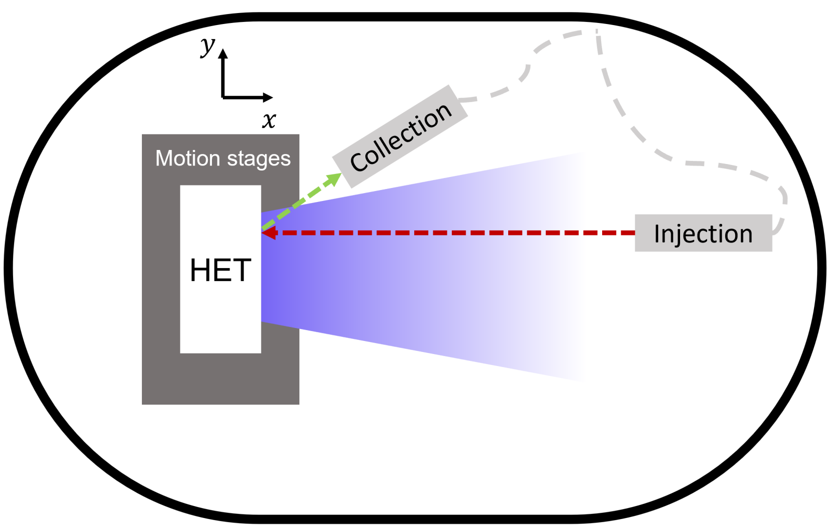

Fig. 3 Optical setup for axial LIF inside the vacuum chamber, with excitation wavelength shown in red and fluorescence wavelength shown in green.

Inside the chamber, we had an 2-inch diameter injection lens with a focal length of 10 cm mounted approximately 10 thruster diameters downstream pointing in the axial direction and a 3-inch diameter collection lens with a focal length of 20 cm mounted slightly downstream and out of the plume of the thruster. At atmosphere, we aligned the optics using visible lasers to ensure that the collection and injection optics were focused on the same alignment spot on the thruster. Each optic was equipped with a small motion stage that allowed us to adjust their positions when the chamber was pumped down, improving our alignment to the spot on the thruster. The thruster was mounted on a motion stage that allowed us to vary the interrogation point, as shown in Fig. 3.

Once collected by the collection optic, the fluoresced light was passed through a bandpass filter centered at 473 nm for krypton and two bandpass filters at 540 and 546 nm for xenon to reduce the noise in our signal. This light was converted to current using a Hamamatsu E717-500 photomultipler tube and converted to voltage using a Oriel 70710 transimpedance amplifier. Finally, an SRS 810 lock-in amplifier tied to the frequency of the chopper was used to distinguish the fluorescence from the background light. We used an integration time of 300 ms on the lock-in amplifiers and a frequency of 2 kHz for the chopper.

B. Data processing

For each condition, we performed axial LIF along channel centerline from approximately 0.13 thruster channel lengths L_{ch} upstream to 0.53 channel lengths downstream of the exit plane (located at 0). The resolution of these points varies for each condition based on the difficulty of collecting data—for instance, the 600 V krypton condition had rapidly-increasing thruster temperatures, so we took fewer data points to limit operation at this condition. At each location, we measured an ion velocity distribution function (IVDF) by varying the input wavelength, changing the range of velocities based on where the peak of the fluorescence intensity was located.

A two-peak Gaussian fit was performed for each of the IVDFs. For each fit, we calculated the mean and mode for the raw data as well as for the fit. These fits are shown in an example trace for krypton at 300 V, 15 A in Fig. 4. The calculated values of mean and mode velocities are shown with fit uncertainty in Fig. 5a.

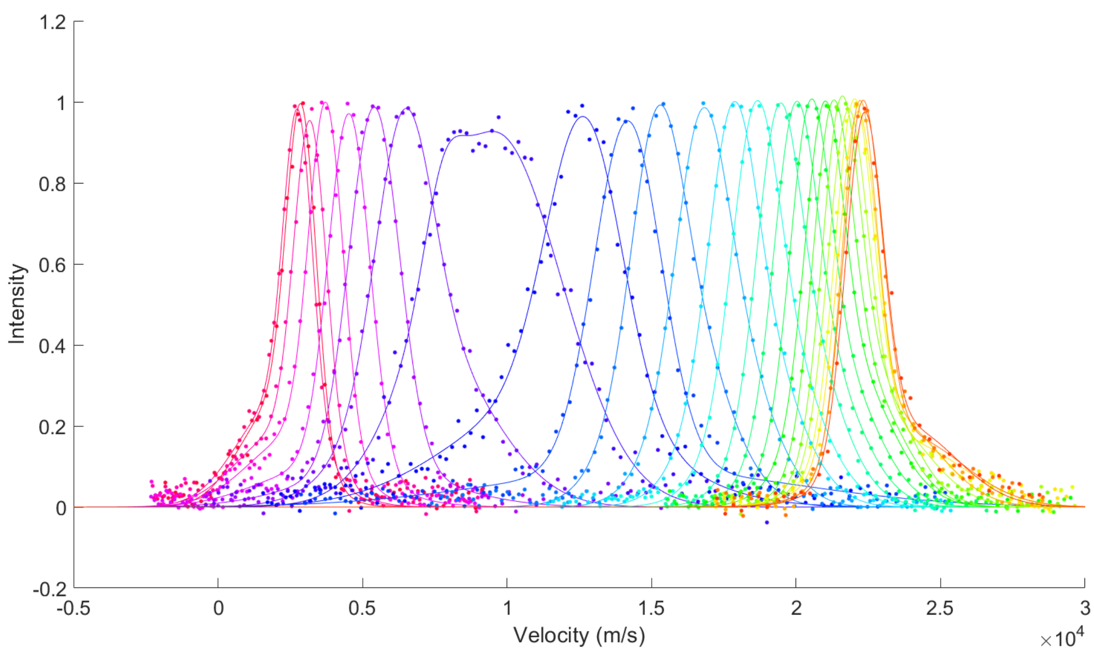

Fig. 4 Ion velocity distribution functions taken along channel centerline at 300 V, 15 A from upstream (purple, low velocities) to downstream (red, high velocities).

To calculate the electric field based on our velocity profile, we use

$$E(z) = \frac{m_i}{q} u(z) \frac{du}{dz}, \tag{1}$$

which assumes no ionization in the acceleration region. While this is not entirely true, as there has been significant overlap between the ionization and acceleration region observed in the past [28], we use this assumption to easily characterize the electric field and acceleration region. We fit a smoothing spline to the fitted mean velocity profile and apply Eq. 1 to obtain the electric field profile. The "location" of the acceleration region is defined as the peak of the electric field, while the "width" is defined as the region over which the electric field is over half of its maximum value.

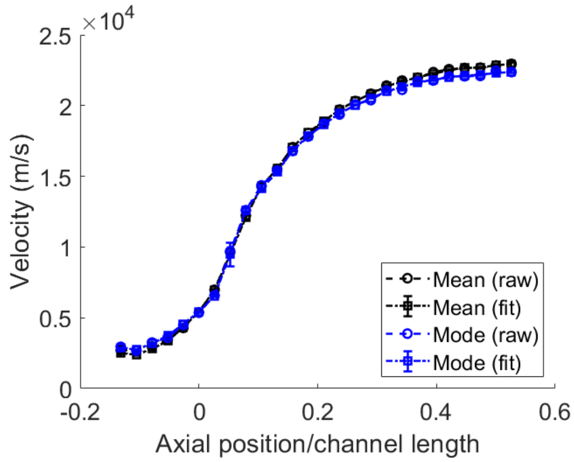

(a)

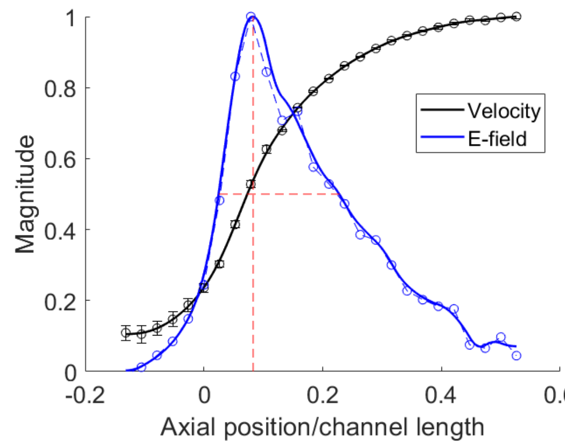

(b)

Fig. 5 Along channel centerline of the H9 operating on krypton at 300 V, 15 A, a) mean and mode of raw and fitted IVDFs shown in Fig.4, and b) mean of fitted ion velocities and electric field. The circular points are the calculated values of mean ion velocities and electric field, while the solid lines represent a smoothing spline fit for the velocity profile and the electric field calculated from that fit.

We performed a bootstrapping analysis to obtain fit uncertainty estimations for each IVDF, with the error bars representing two standard deviations (95%) of the distribution. With this bootstrapping method, we randomly sampled each trace and performed a fit on the resultant profile, repeating this process a thousand times and treating the distribution in the mean and mode velocities as the uncertainty for each [29]. It should also be noted that due to the stark two-peak distribution seen at locations near the exit plane for the 600 V, 15 A xenon condition, slight changes were made to the fit function to force a fit with two distinct peaks, leading to a larger uncertainty in the fit.

C. Simulation setup

We used the measured ion velocity profiles on channel centerline in concert with discharge current measurements to tune the anomalous electron collision frequency profile until the simulated results match the experimental data. In this work, we employ Hall2De, a state-of-the-art fluid axisymmetric Hall thruster code developed at the Jet Propulsion Laboratory [18]. Treating the simulation as a surrogate measurement of the plasma, we can investigate the plasma conditions in the channel and test the main hypothesis put forward in our previous work, i.e. the role of higher electron temperatures in the increasing efficiency gap between xenon and krypton with voltage [13]. However, due the presence of anomalous cross-field electron transport, Hall thruster simulations are not predictive—given only the geometry and operating conditions, we cannot compute the plasma properties and performance without tuning the spatial distribution of the anomalous electron mobility. To this end, we used the mean ion velocity profiles obtained via LIF in the present experimental campaign in conjunction with the measured discharge current to calibrate simulations of the H9 for both xenon and krypton at several operating conditions. We employed a piecewise-linear Bohm-like model for the anomalous collision frequency with eight free parameters, similar to those traditionally employed in Hall2De [15]:

$$\ln\left(\frac{\nu_{AN}(z,\theta)}{\omega_{ce}}\right) = \begin{cases} c_1 & z < z_1 \\ c_1 + c_2\frac{z-z_1}{z_2-z_1} & z_1 \le z < z_2 \\ c_2 + c_3\frac{z-z_2}{z_3-z_2} & z_2 \le z < z_3 \\ c_3 + c_4\frac{z-z_3}{z_4-z_3} & z_3 \le z < z_4 \\ c_4 & z \ge z_4 \end{cases}, \tag{2}$$

where

$$\theta = \{z_1, z_2, z_3, z_4, c_1, c_2, c_3, c_4\}. \tag{3}$$

Running a single Hall2De simulation of the H9 takes between 10 and 20 hours, which makes this calibration a very slow process. To attempt to accelerate this procedure, we employed a new 1D Hall thruster code developed at the University of Michigan, HallThruster.jl [30]. Hall thruster dynamics are suitably one-dimensional that, given an anomalous collision frequency profile, HallThruster.jl will typically predict an ion velocity profile and discharge current that matches the one produced by Hall2De to within 15%. More importantly, although a discrepancy will always exist between the prediction of Hall2De and the prediction of HallThruster.jl due to the latter's lower fidelity, the two codes are well-correlated for this four-zone model. If we alter the anomalous transport profile in a way that steepens the simulated acceleration region or decreases the discharge current in HallThruster.jl, we find that the same behavior will also usually occur in Hall2De, even if their predictions do not match in absolute magnitude. This enabled a workflow in which after each Hall2De simulation, HallThruster.jl was used to propose new points for high-fidelity simulation. This considerably sped up the tuning process.

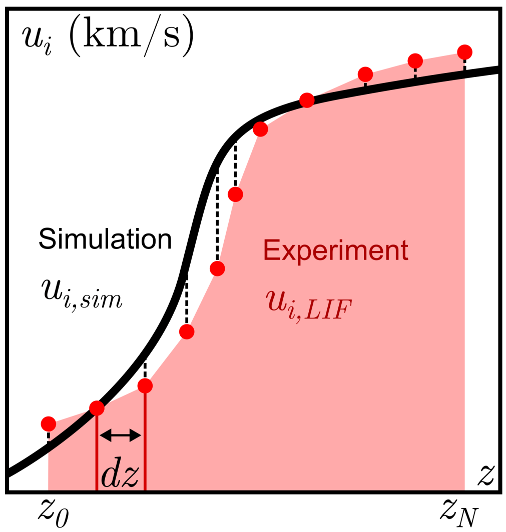

Fig. 6 Diagram of how the integrated velocity error is defined. The numerator of Eq. 4 is the integral of the squared difference (dashed black lines) between the experimental data (red markers) and the simulation (solid black line). The denominator of Eq. 4 is the area denoted in light red. The integral is is performed over the differential length elements integrated by dz from z_0 to z_N.

The results of the calibration procedure are shown in Sec.III.B. We define the integrated velocity error (IVE), a measure of the goodness of fit for our axial velocity profile, as

$$\text{IVE} = \sqrt{\frac{\int_{z_0}^{z_N} (u_{i,LIF}(z) - u_{i,sim}(z,\theta))^2 dz}{\int_{z_0}^{z_N} u_{i,LIF}^2(z) dz}} \tag{4}$$

where $z_{LIF,0}$ and $z_{LIF,N}$ are the axial locations of the first and last LIF data points for the given condition, $u_{i,LIF}$ is the fitted mean ion velocity as determined by LIF, $u_{i,sim}$ is the simulated velocity of the first ion charge state, and θ is the set of model parameters defined in Eq. 3. For this paper, we analyze only the 300 V, 15 A and 600 V, 15 A conditions. We attempted to optimize matching between simulation and experimental data for discharge current and ion velocity profile. While there are other metrics that we could have used to calibrate our data, including thrust and partial efficiencies, we found current and velocity profile to be two of the most intuitive parameters to match. Taking these constant-current conditions at our lowest and highest operating voltage allows us to most succinctly compare the electron temperatures as simulated by Hall2De for krypton and xenon.

III. Results

In this section we present the acceleration profiles for each operating condition and propellant as inferred from laser-induced fluorescence measurements, as well as the comparison between experimental results and calibrated simulation results for the profiles at 300 and 600 V.

A. Ion velocity distribution functions along centerline

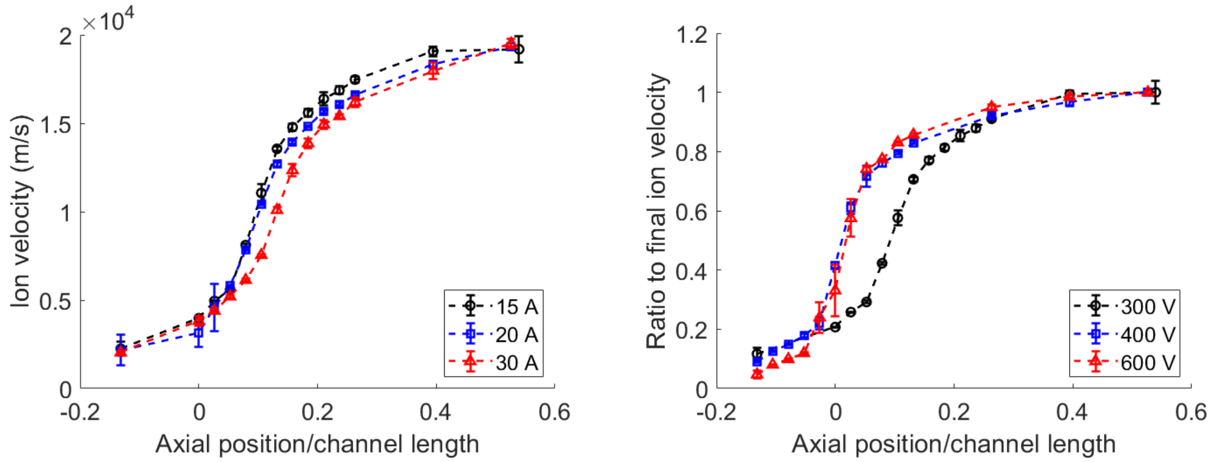

(a) (b)

Fig. 7 Mean xenon ion velocities as calculated from fitted ion velocity distribution functions at various axial locations along thruster channel centerline. Ion velocity profiles are shown with a) increasing discharge current with constant voltage at 300 V and b) increasing discharge voltage with constant current at 15 A.

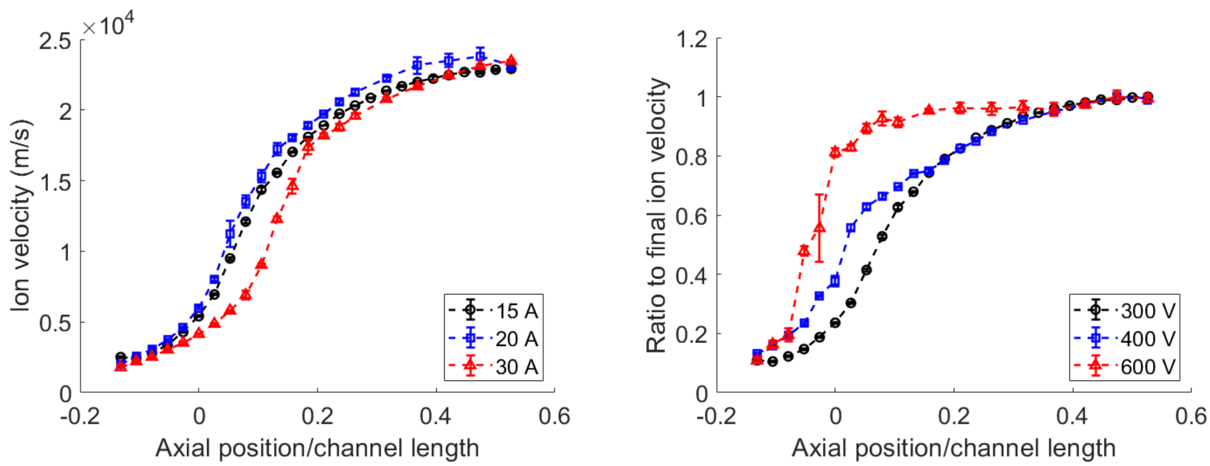

(a) (b)

Fig. 8 Mean krypton ion velocities as calculated from fitted ion velocity distribution functions at various axial locations along thruster channel centerline. Ion velocity profiles are shown with a) increasing discharge current with constant voltage at 300 V and b) increasing discharge voltage with constant current at 15 A.

In this section we show the mean ion velocities calculated from the fitted IVDFs along centerline for all conditions and propellants. We also show the center and width of the acceleration profile as defined in Sec. II.B. For ease of comparison at differing discharge voltages, we scale these acceleration profiles to final ion velocities. First, we present the acceleration profiles calculated at differing all conditions for the H9 operating on xenon in Fig. 7.

With increasing current, the acceleration profile shows minimal change. There is a slight shift downstream at the high-current (30 A) condition, but the shift is on the order of ~1-2 mm. The width of the acceleration profile also appears to stay relatively constant. With increasing voltage, we see an upstream shift in the profile from 300 to 400 V, while the difference between 400 and 600 V is negligible. The profile also appears to steepen slightly at the higher voltage conditions. These trends generally match what has been previously observed for Hall thrusters operating on xenon, both unshielded [17, 31] and shielded [32].

Next, we show in Fig. 8 the mean ion velocities calculated for krypton. As with xenon, the krypton acceleration profile is slightly shifted downstream at 30 A compared to the lower-current conditions, although in the case of krypton, the high-current conditions also appear to have steeper acceleration profiles. We see the same general trend with increasing voltage as xenon in that the acceleration profile steepens and moves upstream. However, where the 400 and 600 V conditions for xenon were nearly identical on xenon, we see that the 400 V condition for krypton represents a distinct "middle ground" between the 300 and 600 V conditions. The trend in the width of the acceleration profile is opposite what has been observed previously on unshielded thrusters, where an increase in voltage resulted in a slight narrowing of the acceleration region rather than a broadening [33]. Additionally, Ref. [33] also indicates that the acceleration region moves downstream at higher voltages for krypton, while we observed a steady upstream shift.

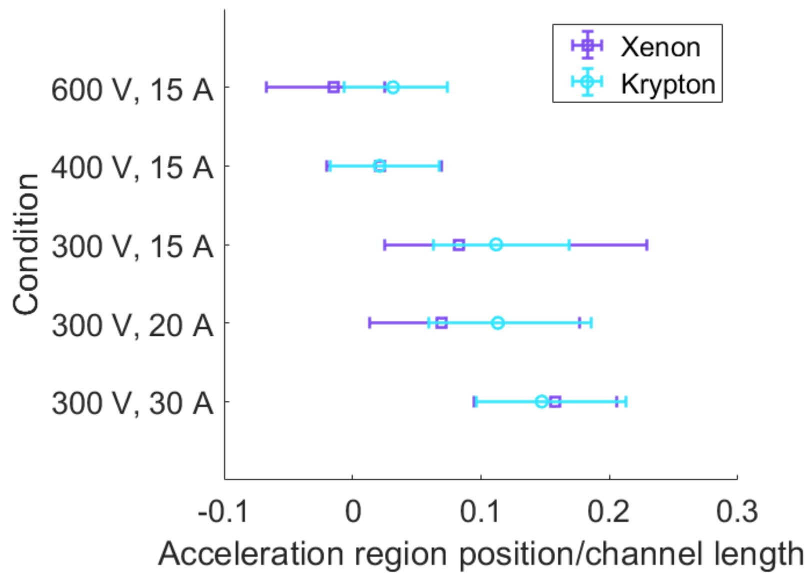

Fig. 9 Acceleration region locations and widths as calculated by Eq. 1 for xenon and krypton at different operating conditions.

Using the definitions outlined in Sec. II.B, we show in Fig. 9 the locations and widths for krypton and xenon at each operating condition. Note that "error bars" represent the width of the acceleration region, not uncertainty in the data. It becomes more apparent from Fig. 9 that the width of the acceleration region for krypton is distinctly decreasing as we increase current. This trend is not the case for xenon, where the acceleration region width stays relatively constant with increasing width. We discuss why these trends may be opposite in Sec. IV.A. Figure 9 also emphasizes the trend in the krypton profile of narrowing and moving upstream continuously with higher voltage, while the xenon profile between 400 and 600 V is nearly identical. The furthest upstream acceleration zone location relative to all other conditions with the same propellant is at 600 V, 15 A for krypton and 400 V, 15 A for xenon, while the furthest downstream location is at 300 V, 30 A for both propellants.

B. Comparison of experimental and simulated data

In Table 3, we present the discharge currents and integrated velocity errors produced by the simulation for each condition. Our initial convergence requirements were to be within 0.5 A of the correct discharge currents with an IVE of less than 0.1. We achieved this tolerance at the 300 V conditions. However, we relaxed our current convergence tolerance for the 600 V cases to 2 A due to the difficulty of obtaining a good fit with only a four-zone Bohm model.

Propellant	Discharge voltage (V)	Simulated current (A)	IVE
Xenon	300	15.1	0.081
Krypton	300	15.3	0.051
Xenon	600	13.3	0.084
Krypton	600	14.5	0.081

Table 3 Simulated current values and integrated velocity errors from Hall2De for both propellants at the 300 and 600 V, 15 A condition.

We extracted the axial ion velocities from the Hall2De results and compared them to the experimental values derived from LIF measurements. By iterating multiple times with different calibration coefficients of the transport profile, we were able to obtain close matches in both current and acceleration profile. The comparison of experimental and simulated acceleration profiles for the 300 V, 15 A condition is shown in Fig. 10a and 10b.

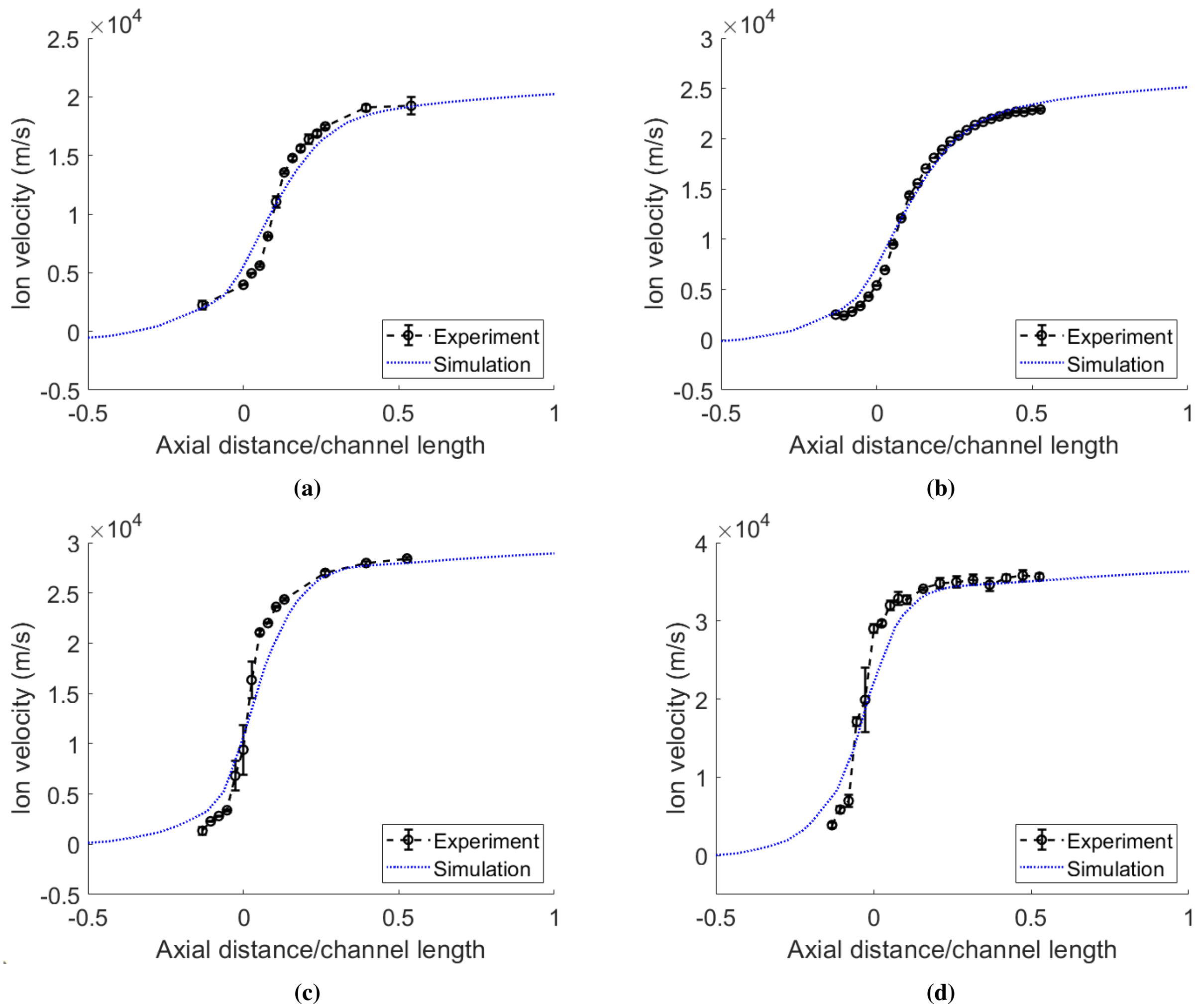

Fig. 10 Experimentally measured and simulated axial ion velocities along channel centerline at a) 300 V, 15 A for xenon, b) 300 V, 15 A for krypton, c) 600 V, 15 A for xenon, and d) 600 V, 15 A for krypton.

Although the simulation results do not entirely lie within the error bars of the experimental data, we still see a close match in the shape of the profile, i.e. where the inflection points are and what velocities the ions ultimately attain. It should be reiterated that the uncertainties are only for the fit of the two-peak Gaussian to the IVDF (Fig. 4), and the true error is likely larger. For both propellants, the experimental ion velocity profile is steeper than the simulated. We show the final calibrated anomalous collision frequency profiles in Fig. 11a.

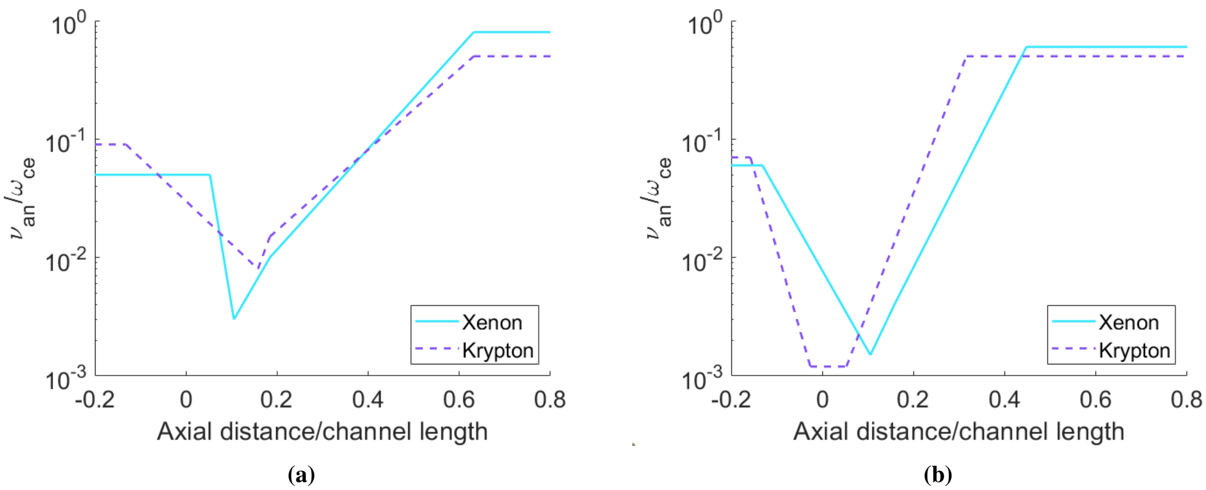

Fig. 11 Best-fit profiles for ratio of anomalous electron collision frequency to electron cyclotron frequency as a function of axial distance along channel centerline for both propellants at a) 300 V, 15 A and b) 600 V, 15 A.

We next turn to the 600 V condition, with the comparison of simulated and experimental ion velocity profile shown in Fig. 10c and 10d. As was the case with the 300 V conditions, the simulated profiles are still slightly too relaxed in comparison to the experimental profiles. In addition, the simulated currents for the 600 V cases were both slightly too low as seen in Table 3. The best anomalous electron collision profile for these cases is seen in Fig. 11b.

In this section, we have shown that our calibrated simulations were able to achieve a discharge current within 2 A of the experimental current. Additionally, we were able to qualitatively capture the correct inflection points of the ion velocity profiles and minimized the integrated velocity distribution. We can use the other plasma parameters of these calibrated Hall2De simulations to further investigate our theories regarding the efficiency gap between propellants at high voltages, which we discuss in Sec.IV.B.

IV. Discussion

In this section, we will discuss the general trends we have observed in the acceleration profile for each propellant with changing operating conditions, as well as the results from our best-fit Hall2De simulations and what insight they may reveal as to the performance disparity between xenon and krypton at high voltages.

A. Acceleration profile trends with increasing power

Although the acceleration region shifts upstream and narrows for both propellants as seen in Fig. 7b and 8b, there are differences in their behaviors at high currents. From 400 to 600 V, the krypton acceleration region continues to narrow and shift upstream, while the xenon acceleration region is nearly identical.

As previously mentioned in Sec. III.A, the acceleration profile widens at high currents for krypton but not for xenon. To understand why we may be observing this behavior, we perform a simple analysis with strong assumptions. We begin with generalized Ohm's law for electrons at steady-state with no pressure gradient and including a collision term:

$$0 = -qn_e\left(\vec{E} + \vec{u}_e \times \vec{B}\right) - m_e n_e \nu_e u_e. \tag{5}$$

Solving through, we find that the electron current density in the axial direction (perpendicular to $\vec{B}$) is

$$j_e = \frac{E}{\eta\left({\Omega_e}^2 + 1\right)}, \tag{6}$$

where η is the plasma resistivity,

$$\eta = \frac{m_e \nu_e}{q^2 n_e}, \tag{7}$$

and Ω_e is the Hall parameter,

$$\Omega_e = \frac{\omega_{ce}}{\nu_e}, \tag{8}$$

where ω_{ce} is the electron cyclotron frequency,

$$\omega_{ce} = \frac{qB}{m_e}, \tag{9}$$

and ν_e is the electron collision frequency.

When $\Omega_e \gg 1$, as it typically is in the channel of a Hall thruster, Eq. 6 simplifies to

$$j_e = \frac{E}{\eta {\Omega_e}^2} = \frac{q^2 n_e \nu_e}{m_e {\omega_{ce}}^2} E. \tag{10}$$

We can approximate the strength of the electric field E as $\frac{V_d}{l}$, where V_d is the discharge voltage and l is the width of the acceleration region. We can then write out Eq. 10 as

$$j_e = \frac{q^2 n_e \nu_e}{m_e {\omega_{ce}}^2} \frac{V_d}{l} = \frac{n_e \nu_e}{B^2} \frac{V_d}{l}. \tag{11}$$

Assuming that the magnetic field stays constant and rearranging, we then have

$$l \propto \frac{n_e \nu_e V_d}{j_e}. \tag{12}$$

We find two different relations for the scaling of the acceleration region width: one with discharge voltage and one with discharge current. For the relationship with voltage, we invoke the following assumptions and assume that n_e and j_e stay the same:

- The discharge voltage is proportional to electron temperature, $V_d \propto T_e$,
- The electron collision frequency is dominated by Coulombic electron-ion collisions, which scale as $\nu_{ei} \approx \nu_e \propto {T_e}^{-3/2}$.

With these assumptions, Eq. 12 reduces to

$$l \propto {V_d}^{-1/2}. \tag{13}$$

For the relationship with current, we invoke the following assumptions and assume that V_d stays the same:

- The discharge current is proportional to electron current density, $I_d \propto j_e$,
- The discharge current is proportional to electron number density, $I_d \propto n_e$,
- The electron collision frequency is a function of the discharge current, $\nu_e = f(I_d)$.

With these assumptions, Eq. 12 reduces to

$$l \propto \nu_e(I_d). \tag{14}$$

Based on this simplified analysis, the acceleration region width decreases with increasing discharge voltage, which we do see with voltage for both xenon and krypton. However, we see that while the width of the acceleration profile of xenon stays relatively constant with increasing current, the profile of krypton steepens rather than relaxes. This implies that the electron collision frequency of krypton is *decreasing* at higher discharge currents, while the electron collision frequency of xenon stays relatively constant. As we improve our calibration procedure between simulation and experimental data, we may use Hall2De to determine whether or not this theory is true by comparing the electron collision frequency profile for xenon and krypton at high currents.

B. Mass utilization efficiency at high voltage

In our previous work, we hypothesize that the efficiency gap between krypton and xenon does not close at high voltages due to the non-linear dependence of ionization cross-section on electron temperature [13]. Unshielded Hall thrusters, which do see the efficiency gap close at high voltages [5], have lower electron temperatures than magnetically shielded Hall thrusters [34]. At lower electron temperatures, the ionization cross-section of krypton increases by a larger margin than xenon over the same increase in electron temperature. At higher electron temperatures, the ionization cross-sections of krypton and xenon increase at approximately the same rate. However, the mass utilization efficiency—which is attributed as the driving factor for the efficiency gap between xenon and krypton—is dependent on more than just the electron temperature. We may use the rate of ion production per unit volume, $\dot{n}_i$, as a proxy for the mass utilization for each propellant. We can define the rate of ion production per unit volume as

$$\dot{n}_i = n_n n_e k_{iz}(T_e), \tag{15}$$

where n_n is the neutral density, n_e is the electron density, and k_{iz} is the ionization rate coefficient, which is dependent on the electron temperature T_e. The densities and electron temperature can be obtained directly from the calibrated Hall2De simulation, while the ionization rate coefficient k_{iz} is found by first assuming a Maxwell-Boltzmann distribution function $f(T_e, \varepsilon)$ for electron temperature over all energies. We then integrate the product of this distribution function, electron velocity, and ionization cross-section over all energies:

$$k_{iz} = \int_0^\infty f(T_e, \varepsilon) u_e(\varepsilon) \sigma_{iz}(\varepsilon) d\varepsilon, \tag{16}$$

where ε is energy, u_e is the electron velocity, and σ_{iz} is the ionization cross-section. The ionization rate coefficient k_{iz} is tabulated such that for we can find its value for any given electron temperature T_e. We extract the densities and electron temperature along channel centerline in Hall2De and compare them between conditions and propellants in Fig. 12.

Across all four cases, the neutral density profile as seen in Fig. 12a is very similar. This is relatively unsurprising, given the similar anode mass flow rates for all cases needed for the same discharge current of 15 A. However, while the electron density profiles (Fig. 12b) have approximately the same shape with a peak at about a third of the way through the channel, the magnitudes of these profiles vary much more drastically. For both krypton and xenon, the peak of electron density increases from 300 to 600 V. However, the peak electron density of xenon increases by 1.89×10^{18} m^{-3}, while the peak for krypton increases by only 1.19×10^{18} m^{-3}.

The shape of the electron temperature profiles (Fig. 12c) qualitatively match the characteristics of the acceleration region (Fig. 9). Generally, the 600 V electron temperature profiles are steeper than the 300 V profiles, which manifests as a narrower acceleration region. We see that at 300 V, the krypton and xenon electron temperatures peak in approximately the same location, but the distribution of krypton is wider than that of xenon. This matches with the trends in acceleration region location and width seen in Fig. 9. For the 600 V case, the peak of the krypton electron temperature profile is upstream of the peak for xenon, just as the krypton acceleration region is upstream of xenon's. Additionally, as is the case with the electron densities, the peak electron temperature of xenon increases more between 300 and 600 V than xenon. Xenon increases by 38.2 eV, while krypton increases by 36.8 eV.

Finally, we can compare the ion production rate per unit volume at each condition in Fig. 12d. Once again, while each of the profiles have a peak upstream of the channel exit plane at $z = 0$, the change between the 300 V and 600 V xenon profiles is much more drastic than that of krypton. The maximum ion production rate per unit volume of xenon increases by 2.5×10^{23} m^{-3}s^{-1}, while the maximum rate for krypton increases by only 1.9×10^{23} m^{-3}s^{-1}. Qualitatively, this disparity in ion production rate per volume may manifest as a larger improvement in mass utilization for xenon with increasing voltage as compared to krypton. Additionally, the peak of ion production for xenon at 600 V is significantly upstream compared to the other conditions—high-voltage xenon peaks at 0.8 channel lengths upstream of the exit plane, while the other three conditions peak between 0.4 and 0.3 L_{ch} upstream. This upstream shift may improve the divergence efficiency of xenon, as more ions are born upstream and therefore accelerated axially out of the channel. Indeed, we see from our previous work in Ref. [13] that between 300 V and 400 V, the divergence efficiency of xenon improves by 1.9 ± 2.7%, while the divergence efficiency of krypton *worsens* by 0.7 ± 1.2%. While these differences are minor and have relatively high uncertainty, they match our expectations for how the divergence would scale with increasing discharge voltage for each propellant based on the shape of the ionization rate profiles seen in Fig. 12d.

To quantitatively characterize the difference in trends for the mass utilization efficiency, we can express the ion beam mass flow rate $\dot{m}_b$ as the rate of ion production per unit volume integrated over the volume of the channel:

$$\dot{m}_b = \int_V m_i \dot{n}_i dV = 2\pi m_i \int_0^{z_{end}} \int_{r_i}^{r_o} \dot{n}_i(r, z) r dr dz, \tag{17}$$

where we assume an axisymmetric distribution and integrate over the width of the channel radially. As Hall2De uses individual cells with varying sizes to calculate its plasma parameters, we calculate this integral as

$$\dot{m}_b = \sum_{r=r_i, z=0}^{r=r_o, z=z_{end}} \dot{n}_i(r, z) r \Delta r \Delta z. \tag{18}$$

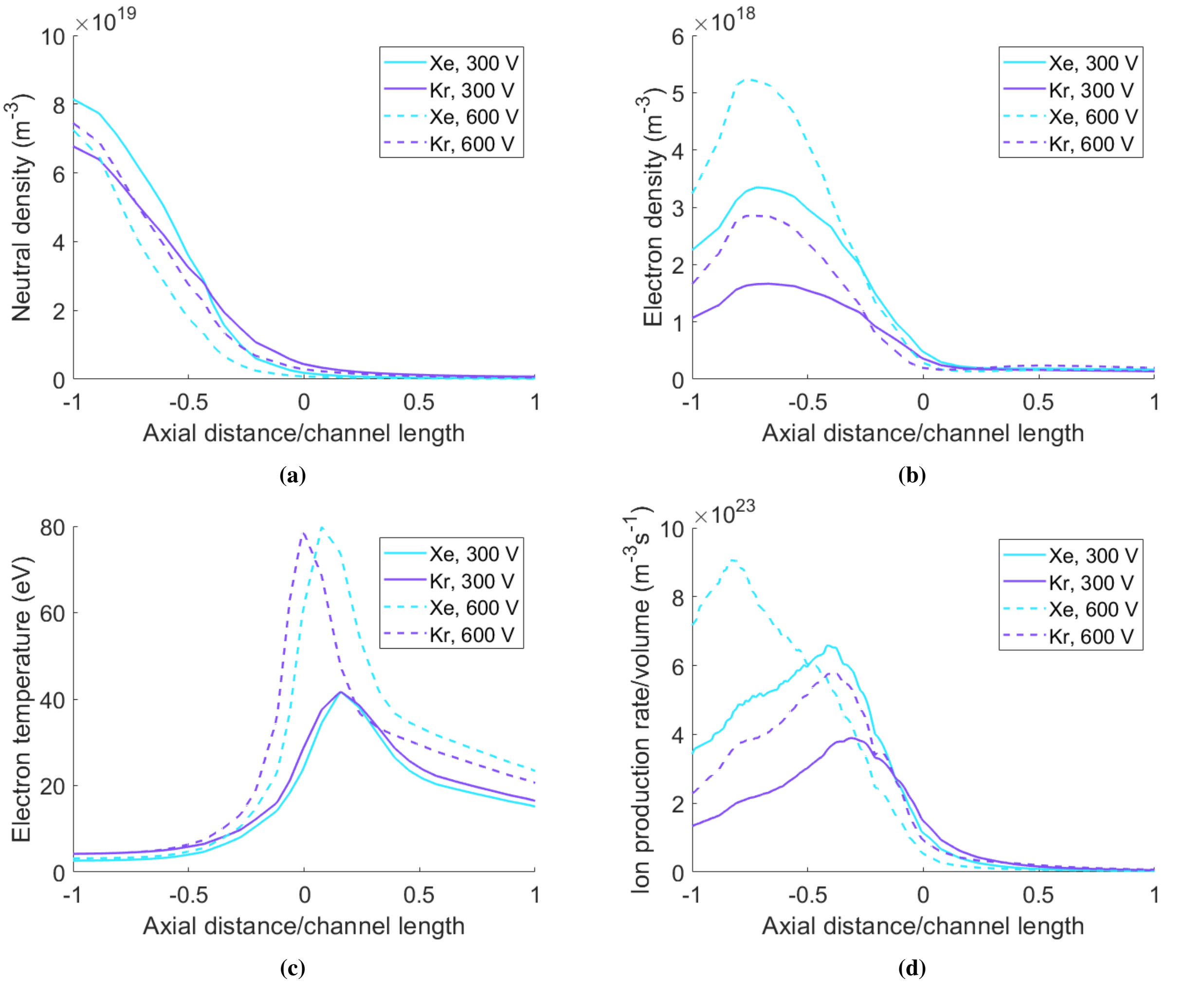

Fig. 12 Values of a) neutral density, b) electron density, c) electron temperature, and b) rate of ion production per unit volume for xenon and krypton at 300 V and 600 V determined from calibrated Hall2De simulations. The 0 on the x axis indicates the exit plane of the channel, while -1 indicates the position of the anode.

Armed with these formulations, we may then calculate the mass utilization efficiency as $\eta_m = \frac{\dot{m}_b}{\dot{m}_a}$, where $\dot{m}_a$ is the neutral anode mass flow rate taken from Ref. [13]. One challenge with this definition of ion beam mass flow rate is determining the axial integration bound z_{end}. In order to properly capture all beam ions, we must extend our integration volume beyond the exit plane as significant ionization is still happening downstream (see Fig. 12d). However, we define the beam ions of a Hall thruster as the population of high-energy ions leaving the thruster channel. We therefore wish to exclude the low-energy charge exchange ions that may result from background pressure [35], as Hall2De does account for these facility effects. We therefore may not place our end bound arbitrarily far downstream. As we do not know the exact downstream bound, we instead calculate the efficiency of mass utilization ratios between xenon and krypton for multiple selections of our integration bound z_{end}. We use this ratio of simulated mass utilization efficiencies as a proxy for the ratio of overall anode efficiencies, i.e. $\frac{\eta_m|_{Xe}}{\eta_m|_{Kr}} \approx \frac{\eta_a|_{Xe}}{\eta_a|_{Kr}}$. We then compare these anode efficiency ratios to the ratios calculated from our experimental measurements [13].

Figure 13 indicates that with a selected integration bound of one channel length downstream of the exit plane, we calculate simulated ratios of efficiencies, $\frac{\eta_{xe}}{\eta_{kr}}$, that fall within the uncertainty of the experimental ratios. The implications of this result are that given a proper integration bound, we are able to attribute the discrepancy in efficiency gap between xenon and krypton to the differences in the ion production rate per unit volume $\dot{n}_i$ (Fig. 12d), where the rate of xenon ion production increases more drastically at high voltages compared to krypton. In turn, the differences in ion production rate profile are due to the larger increases for xenon in both electron temperature and electron density when scaling to

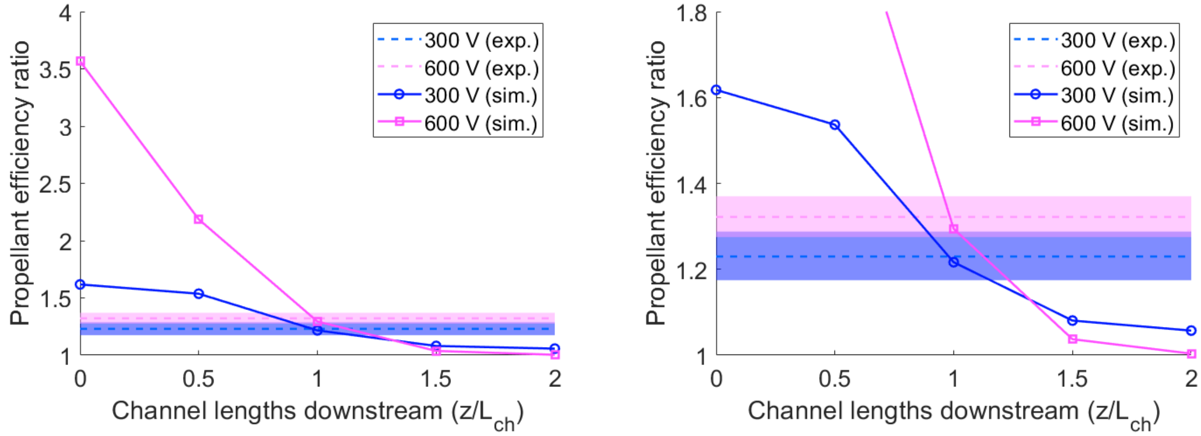

(a)

(b)

Fig. 13 Ratio of anode efficiencies between xenon and krypton (η_{xe}/η_{kr}) for different discharge voltages calculated from simulation (Eq. 17) and experiment (Ref. [13]) based on axial integration bound z_{end}. Shaded regions represent uncertainty in the experimental values. The range of ratios is chosen to show a) the full range of calculated ratios and b) the local area around experimentally calculated ratios.

high voltage. This trend does match our hypothesis from Ref. [13] and introduces the importance of electron density in the efficiency gap. Although out of the scope of this work, we expect that the lower electron temperature ranges seen for unshielded Hall thrusters [34] are at least partially responsible for the closing gap in efficiency between xenon and krypton at high voltages.

One caveat to note is that the actual efficiencies calculated from simulation were too low by an order of magnitude, i.e. in the range of 5% or less. However, our focus is not on the absolute values of these efficiencies but instead on the scaling with voltage, and we see that the scaling of efficiency ratios from our simulations matches the scaling seen from experimental measurements.

V. Conclusion

In this work, we characterize the efficiency gap between xenon and krypton performance at varying operating conditions through experimental measurements of ion velocity profile and calibrated simulations. We measured ion velocity profiles axially along channel centerline with laser-induced fluorsence, a non-invasive optical diagnostic, at multiple operating conditions for both xenon and krypton. We observe similar behavior in the location of the xenon and krypton acceleration regions with increasing voltage and current, matching previous work done on unshielded and shielded thrusters. We also used generalized Ohm's law with a number of strong assumptions to find scaling laws for the width of the acceleration region at varying conditions, revealing that the electron collision frequency of krypton may decrease at high currents while remaining relatively constant for xenon.

We then calibrated simulations from Hall2De, a multi-fluid Hall thruster code, by matching both discharge current and ion velocity profile for the 300 V and 600 V conditions. We were able to calibrate our 300 V simulations to discharge currents within 0.5 A of experiment and our 600 V simulations to discharge currents with 2 A of experiment. For all four cases, our integrated velocity error was under 0.1. The results from our calibrated Hall2De simulations showed that the electron temperature profile and electron density profile increase more drastically for xenon than they do for krypton with increasing voltages. In turn, we see a larger increase in the rate of ion production per unit volume at high voltages for xenon than we do for krypton. Finally, we calculate the ratio of mass utilization efficiencies between propellants at each voltage from our simulation results and, using them as a proxy for anode efficiencies, compare to experimental data. We find that given a certain integration bound, we are able to obtain simulated efficiency ratios at each voltage that fall within the uncertainty of our experimental results.

To our knowledge, this work represents the first use of laser-induced fluorescence on a magnetically shielded Hall thruster operating on krypton. Additionally, it is the first time Hall2De has been calibrated on shielded krypton operation. Our results and discussion indicate that the increasing gap between xenon and krypton efficiencies at high voltages on shielded thrusters is due to the larger increase in ion production rate per unit volume for xenon compared to krypton. As the use of krypton on magnetically shielded Hall thrusters becomes more imperative due to the rising cost of xenon and the long-duration tests needed for deep space missions, it is critical that we characterize the driving physics of the performance gap between xenon and krypton. This work represents an important step forward in our understanding of the underlying factors for the disparity in xenon and krypton operation, informing future work that may improve the performance of these devices.

References

[1] "Space Nuclear Propulsion for Human Mars Exploration." Tech. rep., National Academies of Sciences, Engineering, and Medicine, Washington, DC, 2021.

[2] Herman, D. A., and Unfried, K. G., "Xenon Acquisition Strategies for High Power Electric Propulsion NASA Missions," *Joint Army Navy NASA Air Force*, Nashville, TN, 2015.

[3] Bugrova, A. I., Bishaev, A. M., Desyatskov, A. V., Kozintseva, M. V., Lipatov, A. S., and Dudeck, M., "Experimental investigations of a krypton stationary plasma thruster," *Int. J. Aerosp. Eng.*, 2013, p. 686132. https://doi.org/10.1155/2013/686132.

[4] Kurzyna, J., Jakubczak, M., Szelecka, A., and Dannenmayer, K., "Performance tests of IPPLM's krypton Hall thruster," *Laser Part. Beams*, Vol. 36, No. 1, 2018, pp. 105–114. https://doi.org/10.1017/S0263034618000046.

[5] Hofer, R. R., Peterson, P. Y., Jacobson, D. T., and Manzella, D. M., "Factors Affecting the Efficiency of Krypton Hall Thrusters," *46th Meeting of the APS Division of Plasma Physics*, Savannah, GA, 2004.

[6] Linnell, J. A., and Gallimore, A. D., "Efficiency Analysis of a Hall Thruster Operating with Krypton and Xenon," *J. Propul. Power*, Vol. 22, No. 6, 2006, pp. 1402–1418.

[7] Kamhawi, H., Haag, T., Jacobson, D., and Manzella, D., "Performance Evaluation of the NASA-300M 20 kW Hall Thruster," *47th Joint Propulsion Conference and Exhibit*, American Institute of Aeronautics and Astronautics, San Diego, CA, 2011.

[8] Peterson, P., Jacobson, D., Manzella, D., and John, J., "The Performance and Wear Characterization of a High-Power High-Isp NASA Hall Thruster," *41st Joint Propulsion Conference and Exhibit*, American Institute of Aeronautics and Astronautics, Tucson, AZ, 2005. https://doi.org/10.2514/6.2005-4243.

[9] Marrese, C., Gallimore, A. D., Haas, J., Foster, J., King, B., Kim, S. W., and Khartov, S., "An investigation of stationary plasma thruster performance with krypton propellant," *31st Joint Propulsion Conference and Exhibit*, American Institute of Aeronautics and Astronautics, 1995. https://doi.org/10.2514/6.1995-2932.

[10] Jacobson, D. T., and Manzella, D. H., "50 kW Class Krypton Hall Thruster Performance," *39th Joint Propulsion Conference and Exhibit*, NASA, Huntsville, Alabama, 2003.

[11] Mikellides, I. G., Katz, I., Hofer, R. R., and Goebel, D. M., "Magnetic shielding of a laboratory Hall thruster. I. Theory and validation," *J. Appl. Phys.*, Vol. 115, No. 4, 2014, p. 043303. https://doi.org/10.1063/1.4862313.

[12] Hofer, R. R., Goebel, D. M., Mikellides, I. G., and Katz, I., "Magnetic shielding of a laboratory Hall thruster. II. Experiments," *J. Appl. Phys.*, Vol. 115, No. 4, 2014, p. 043304. https://doi.org/10.1063/1.4862314.

[13] Su, L. L., and Jorns, B. A., "Performance comparison of a 9-kW magnetically shielded Hall thruster operating on xenon and krypton," *Journal of Applied Physics*, Vol. 130, No. 16, 2021, p. 163306. https://doi.org/10.1063/5.0066849.

[14] Jorns, B. A., Goebel, D. M., and Hofer, R. R., "Plasma perturbations in high-speed probing of hall thruster discharge chambers: Quantification and mitigation," *51st AIAA/SAE/ASEE Joint Propulsion Conference*, American Institute of Aeronautics and Astronautics Inc, AIAA, 2015. https://doi.org/10.2514/6.2015-4006.

[15] Mikellides, I. G., and Lopez Ortega, A., "Challenges in the development and verification of first-principles models in Hall-effect thruster simulations that are based on anomalous resistivity and generalized Ohm's law," *Plasma Sources Science and Technology*, Vol. 28, No. 1, 2019. https://doi.org/10.1088/1361-6595/aae63b.

[16] Cedolin, R. J., Hargus, W. A., Storm, P. V., Hanson, R. K., and Cappelli, M. A., "Laser-induced fluorescence study of a xenon Hall thruster," *Applied Physics B: Lasers and Optics*, Vol. 65, 1997, pp. 459–469.

[17] Hargus, W. A., and Cappelli, M. A., "Laser-induced fluorescence measurements of velocity within a Hall discharge," *Applied Physics B: Lasers and Optics*, Vol. 72, No. 8, 2001, pp. 961–969. https://doi.org/10.1007/s003400100589.

[18] Mikellides, I. G., and Katz, I., "Numerical simulations of Hall-effect plasma accelerators on a magnetic-field-aligned mesh," *Physical Review E - Statistical, Nonlinear, and Soft Matter Physics*, Vol. 86, No. 4, 2012.

[19] Hofer, R. R., Cusson, S. E., Lobbia, R. B., and Gallimore, A. D., "The H9 Magnetically Shielded Hall Thruster," *35th International Electric Propulsion Conference*, Atlanta, GA, 2017.

[20] Cusson, S. E., Hofer, R. R., Lobbia, R., Jorns, B. A., and Gallimore, A. D., "Performance of the H9 Magnetically Shielded Hall Thrusters," *35th International Electric Propulsion Conference*, Atlanta, Georgia, 2017.

[21] Hofer, R. R., Goebel, D. M., and Walker, R. M., "Compact Lab6 Hollow Cathode for a 6-kW Hall Thruster," *54th JANNAF Propulsion Meeting*, 2018, pp. 14–17.

[22] Peterson, P. Y., Kamhawi, H., Huang, W., Yim, J., Herman, D., Williams, G., Gilland, J., and Hofer, R., "NASA HERMeS hall thruster electrical configuration characterization," *52nd Joint Propulsion Conference*, 2016. https://doi.org/10.2514/6.2016-5027.

[23] Viges, E. A., Jorns, B. A., Gallimore, A. D., and Sheehan, J. P., "University of Michigan's Upgraded Large Vacuum Test

Facility," *36th International Electric Propulsion Conference*, Vienna, Austria, 2019.
[24] Dankanich, J. W., Walker, M., Swiatek, M. W., and Yim, J. T., "Recommended practice for pressure measurement and calculation of effective pumping speed in electric propulsion testing," *J. Propul. Power*, Vol. 33, No. 3, 2017, pp. 668–680. https://doi.org/10.2514/1.B35478.
[25] Kramida, A., Yu. Ralchenko, Reader, J., and and NIST ASD Team, NIST Atomic Spectra Database (ver. 5.9), [Online]. Available: `https://physics.nist.gov/asd` [2022, April 5]. National Institute of Standards and Technology, Gaithersburg, MD., 2021.
[26] Hargus, W. A., Azarnia, G. M., and Nakles, M. R., "Demonstration of Laser-Induced Fluorescence on a Krypton Hall Effect Thruster," *32nd International Electric Propulsion Conference*, Wiesbaden, Germany, 2011.
[27] Dale, E. T., "Investigation of the Hall Thruster Breathing Mode," Ph.D. thesis, University of Michigan, Ann Arbor, 2020.
[28] Dale, E. T., and Jorns, B. A., "Two-zone Hall thruster breathing mode mechanism, Part II: Experiment," *36th International Electric Propulsion Conference*, Vienna, Austria, 2019.
[29] Efron, B., and Tibshirani, R. J., CRC Press, 1994.
[30] Marks, T. A., Schedler, P., and Jorns, B. A., "HallThruster.jl - An open source 1D fluid Hall thruster code," , 2022. https://doi.org/10.5281/zenodo.6614275, URL https://github.com/UM-PEPL/HallThruster.jl.
[31] Gawron, D., Mazouffre, S., Sadeghi, N., and Héron, A., "Influence of magnetic field and discharge voltage on the acceleration layer features in a Hall effect thruster," *Plasma Sources Science and Technology*, Vol. 17, No. 2, 2008, pp. 0–10. https://doi.org/10.1088/0963-0252/17/2/025001.
[32] Chaplin, V. H., Jorns, B. A., Lopez Ortega, A., Mikellides, I. G., Conversano, R. W., Lobbia, R. B., and Hofer, R. R., "Laser-induced fluorescence measurements of acceleration zone scaling in the 12.5 kW HERMeS Hall thruster," *Journal of Applied Physics*, Vol. 124, No. 18, 2018. https://doi.org/10.1063/1.5040388.
[33] Linnell, J. A., and Gallimore, A. D., "Internal plasma potential measurements of a Hall thruster using xenon and krypton propellant," *Phys. Plasmas*, Vol. 13, No. 9, 2006. https://doi.org/10.1063/1.2335820.
[34] Hofer, R., Goebel, D., Mikellides, I., and Katz, I., "Design of a Laboratory Hall Thruster with Magnetically Shielded Channel Walls, Phase II: Experiments," *48th Joint Propulsion Conference and Exhibit*, American Institute of Aeronautics and Astronautics, Atlanta, GA, 2012.
[35] Haas, J. M., "Low-Perturbation Interrogation of the Internal and Near-Field Plasma Structure of a Hall Thruster Using a High-Speed Probe Positioning System," Ph.D. thesis, University of Michigan, Ann Arbor, 2001.